




RESEARCH ARTICLE

Multimodality *In Vivo* Imaging of Perfusion and Glycolysis in a Rat Model of C6 Glioma

Qi Qi,^{1,2,3} Matthew S. Fox,^{3,4} Heeseung Lim,^{1,5} Robert Bartha,^{1,5,6}
 Timothy J. Scholl,^{1,2,5,7} Lisa Hoffman,^{1,3,8} Ting-Yim Lee,^{1,2,3,5,6}
 Jonathan D. Thiessen^{1,3,5,6} 

¹Department of Medical Biophysics, The University of Western Ontario, London, ON, N6A 3K7, Canada

²Department of Molecular Imaging Program, The University of Western Ontario, London, ON, N6A 3K7, Canada

³Imaging Program, Lawson Health Research Institute, London, ON, N6A 4V2, Canada

⁴Department of Physics and Astronomy, The University of Western Ontario, London, ON, N6A 3K7, Canada

⁵Robarts Research Institute, The University of Western Ontario, London, ON, N6A 3K7, Canada

⁶Department of Medical Imaging, The University of Western Ontario, London, ON, N6A 3K7, Canada

⁷Ontario Institute for Cancer Research, Toronto, ON, M5G 0A3, Canada

⁸Department of Anatomy and Cell Biology, The University of Western Ontario, London, ON, N6A 3K7, Canada

Abstract

Purpose: Chemical exchange saturation transfer MRI using an infusion of glucose (glucoCEST) is sensitive to the distribution of glucose *in vivo*; however, whether glucoCEST is more related to perfusion or glycolysis is still debatable. We compared glucoCEST to computed tomography perfusion (CTP), [¹⁸F] fluorodeoxyglucose positron emission tomography (FDG-PET), and hyperpolarized [1-¹³C] pyruvate magnetic resonance spectroscopy imaging (MRSI) in a C6 rat model of glioma to determine if glucoCEST is more strongly correlated with measurements of perfusion or glycolysis.

Methods: 10⁶ C6 glioma cells were implanted in Wistar rat brains ($n = 11$). CTP (including blood volume, BV; blood flow, BF; and permeability surface area product, PS) and FDG-PET standardized uptake value (SUV) were acquired at 11 to 13 days post-surgery. GlucoCEST measurements (Δ CEST) were acquired the following day on a 9.4 T MRI before and after an infusion of glucose solution. This was followed by MRSI on a 3.0 T MRI after the injection of hyperpolarized [1-¹³C] pyruvate to generate regional maps of the lactate:pyruvate ratio (Lac:Pyr). Pearson's correlations between glucoCEST, CTP, FDG-PET, and Lac:Pyr ratio were evaluated.

Results: Tumors had significantly higher SUV, BV, and PS than the contralateral brain. Tumor Δ CEST was most strongly correlated with CTP measurements of BV ($\rho = 0.74$, $P = 0.01$) and PS ($\rho = 0.55$, $P = 0.04$). No significant correlation was found between glycolysis measurements of SUV or Lac:Pyr with tumor Δ CEST. PS significantly correlated with SUV ($\rho = 0.58$, $P = 0.005$) and Lac:Pyr ($\rho = 0.75$, $P = 0.005$). BV significantly correlated with Lac:Pyr ($\rho = 0.57$, $P = 0.02$), and BF significantly correlated with SUV ($\rho = 0.49$, $P = 0.02$).

Conclusion: This study determined that glucoCEST is more strongly correlated to measurements of perfusion than glycolysis. GlucoCEST measurements have additional confounds, such as sensitivity to changing pH, that merit additional investigation.

Key words: Glioblastoma, Tumor glycolysis, Tumor perfusion, glucoCEST, FDG-PET, hyperpolarized [$1\text{-}^{13}\text{C}$]pyruvate

Introduction

Glioblastoma multiforme (GBM) is both the most common and the most aggressive type of malignant brain tumor. Regardless of technical advances, the median survival period for patients who are diagnosed with GBM remains approximately 12–15 months [1]. Angiogenesis, the formation of blood vessels, is regarded as one of the hallmarks of GBM. These newly formed vessels facilitate the delivery of nutrients such as glucose to cancer cells, contributing to the observed increase in tumor metabolism (glycolysis) and, ultimately, tumor proliferation [2]. Inevitably, measurements of tumor perfusion and glucose metabolism are interrelated and are important imaging biomarkers for predicting tumor cell proliferation and assessing treatment response. Chemical exchange saturation transfer (CEST), a magnetic resonance imaging (MRI) technique, may be used to monitor both tumor perfusion and glucose metabolism [3]. In particular, CEST is sensitive to endogenous glucose, potentially allowing us to monitor the change in metabolite concentration over time after an injection of glucose (glucoCEST) [4, 5]. Originally, researchers proposed that the change in concentration monitored using glucoCEST in the tumor region was associated with glucose metabolism [6, 7]. However, recent studies have shown that these changes are also sensitive to tumor perfusion [8, 9].

To evaluate glucoCEST as a surrogate biomarker of tumor perfusion and/or tumor glycolysis, we compared various well-defined *in vivo* perfusion and glycolysis measurements in the C6 rat glioma model. Tumor perfusion maps such as blood flow (BF), blood volume (BV), and permeability surface-area product (PS) were derived with computed tomography perfusion (CTP) measurements acquired during a bolus injection of iodinated contrast agent (Isovue). Glucose metabolism was evaluated with positron emission tomography (PET) and ^{18}F -fluorodeoxyglucose (FDG), a glucose analogue which is phosphorylated in the cell but does not go through subsequent steps of glycolysis. Aerobic glycolysis was measured with MR spectroscopic imaging (MRSI) after an injection of hyperpolarized [$1\text{-}^{13}\text{C}$]pyruvate.

Methods

The experimental timeline is shown in Fig. 1a. In short, C6 glioma tumor cells were implanted on day 0. A CT perfusion check was performed on day 7 to check if the diameter of the tumor has reached 4 mm [10–12]. FDG-PET followed by CT perfusion acquisition was performed between days 11 and 13 after C6 cell implantation. GlucoCEST MRI

followed by hyperpolarized [$1\text{-}^{13}\text{C}$] pyruvate MRI experiments was performed on the next day immediately prior to euthanization. All imaging experiments took place within a span of 24 h for each animal: FDG-PET and CT perfusion in the afternoon/evening, followed by 9.4 T MRI (glucoCEST) and 3 T MRI (hyperpolarized MRSI) in the morning/afternoon of the subsequent day. All procedures were performed in compliance with the Canadian Council for Animal Care and approved by the Western University Animal Care Committee.

C6 Glioma Model

Male Wistar rats (Charles River, Canada, age 8 to 10 weeks at surgery) weighing on average 401 ± 42 g ($N = 11$) were used in this study. The animals were induced with 5 % isoflurane and were maintained at 2–3 % for all surgical and imaging procedures.

C6 glioma cells (CCL-107, American Type Culture Collection, Manassas, VA) were cultivated in F12k 15 % horse serum, 2.5 % bovine serum, and 1 % penicillin-streptomycin. Animals were placed into a stereotactic surgical frame during C6 glioma cell implantation. The animals were anesthetized with 2 % isoflurane and were injected with Metacam (Boehringer Ingelheim Vetmedica Inc., Duluth, USA, 10 mg/kg). The bregma was exposed after a scalp incision; a 1-mm-diameter burr hole was drilled at a point 1 mm anterior and 3 mm right of the bregma. A total of 10^6 C6 glioma cells suspended in 10 μL were slowly injected over a period of 5 min at a depth of 3–4 mm from the skull surface with a Hamilton syringe. The burr hole was sealed with bone wax, and the scalp was closed with sutures. The subjects were recovered and returned to animal care housing where they received an additional subcutaneous injection of Metacam (10 mg/kg) 12 h after surgical recovery.

CT Perfusion Imaging and Analysis

Detailed CT perfusion acquisition and analysis procedures can be found in previous research publications [10, 11]. In short, a non-contrast CT scan was performed prior to the perfusion scan to identify sixteen slices covering the entire brain with each section 1.25-mm thick (GE Discovery RCT). CT perfusion data were acquired over two back-to-back time periods. A fine temporal resolution (1.4-s intervals) was used during the first time period (32-s duration), and a coarse temporal resolution (15-s intervals) was used in the second period (165-s duration). Two to 3 s after the start of the first

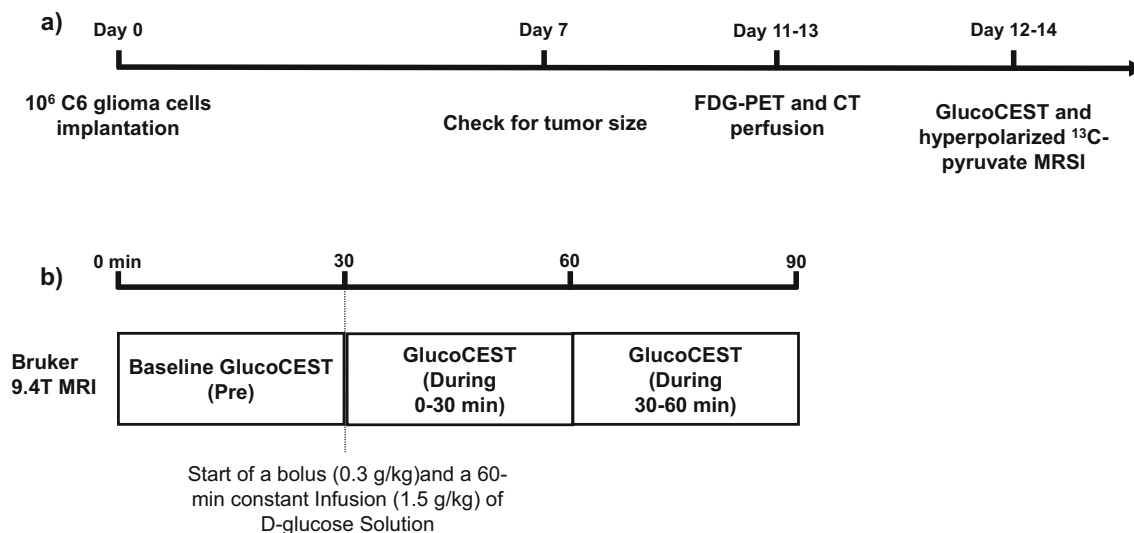


Fig. 1. **a** Study overview. Day 0 corresponds to the tumor cell implantation. A CT perfusion check was performed on day 7 to monitor if the tumor had reached optimal size (diameter > 4 mm). An FDG-PET acquisition followed by CT perfusion experiment was carried out between days 11 and 13. The glucoCEST experiment and hyperpolarized ¹³C-pyruvate MRSI took place on the following day (days 12 to 14). **b** Dynamic CEST experiment. There were three CEST acquisitions: a baseline CEST acquisition (pre), a second CEST acquisition during the first 30 min of glucose infusion (during 1), and a final CEST acquisition during the last 30 min of glucose infusion (during 2).

phase, a bolus of contrast (Iovue, Bracco Diagnostics Inc, Vaughan, Canada, 300 mg iodine/mL, 2.5 mL/kg body weight) was injected into a lateral tail vein at a rate of 0.13 mL/s using a syringe pump (New Era Pump Systems, Inc, Farmingdale, NY, USA). The scan parameters were 80 kVp, 120 mAs, and 10 cm field-of-view with a high-definition bone filter. A change of CT number as a function of time can be measured using the dynamic series of CTP images. The subjects were able to proceed to the subsequent experiments when the axial diameter of the tumor reached 4 mm [11, 12]. The CT perfusion measurements that were used in the perfusion analysis were acquired days 11–13 on a clinical CT scanner (Discovery 750 HD, GE Healthcare, Waukesha, WI) after a 75-min dynamic FDG-PET acquisition.

CT perfusion 5 (GE Healthcare) was used to generate maps of BF, BV, and PS. The time attenuation curve (TAC) from the carotid artery was selected as the arterial input. The arterial TAC was deconvolved with tissue TACs measured from 2 × 2 pixel blocks of CT images using the Johnson-Wilson model to calculate maps of BF, BV, and PS [12, 13]. The tissue enhancement curve can be expressed as the convolution between the blood flow-scaled impulse residue function (IRF), $BF \cdot R(t)$, and the arterial TAC, $C_a(t)$. The shape of the BF-scaled IRF has two distinct phases, and it is solved by deconvolving the arterial TAC with the tissue enhancement curve. The plateau of the BF-scaled IRF defines the BF, while the area under the first phase of the BF-IRF is the BV. The second phase of the BF-scaled IRF starts at the height of the extraction fraction, which is the fraction of contrast agent that leaks into the interstitial space.

The second phase of the BF-scaled IRF decays with time, and PS can be calculated as

$$PS = -BF \times \ln(1-E).$$

FDG-PET Imaging

The FDG-PET acquisition took place 11–13 days after the surgery on a small animal PET system (Inveon DPET, Siemens Healthineers, Knoxville, TN, USA). The blood glucose level of each subject was tested using a glucometer prior to FDG-PET acquisition (CONTOUR meter, Ascensia Diabetes Care, Parsippany, NJ, USA). A 75-min emission scan was performed with a timing window of 3.432 ns and 350–640 keV discrimination energy range. Longitudinal PET data were binned into successive time intervals comprised of 10 frames of 30 s, 5 frames of 60 s, 10 frames of 300 s, and 1 frame of 900 s, totaling 75 min. An iterative, 3D ordered subset expectation maximization (OSEM3D) reconstruction was used to generate dynamic images for all frames with 2 iterations and 18 subsets. Approximately 30 s after the acquisition had started, a bolus of ¹⁸F-FDG (31.5 ± 3.1 MBq) was injected through a lateral tail vein. Anatomical CT images acquired after the PET acquisition were used to generate attenuation corrected PET images. The CT images were co-registered with the PET images using ASIPro (Siemens Healthineers, Knoxville, TN, USA). The

co-registered CT images were used to generate a mu-map by converting Hounsfield units into linear attenuation coefficients for 511 keV gamma rays. The mu-map was then converted into an attenuation sinogram. The PET images were reconstructed using the attenuation sinogram to create the attenuation corrected PET images.

Standardized uptake values (SUV) were calculated using the last 15 min of the dynamic PET images as a surrogate for glucose metabolism. SUV was defined as $SUV = \text{Activity Concentration of ROI} / (\text{Injected Dose} / \text{Weight of the Subject})$ [14].

Dynamic glucoCEST Imaging

MRI was acquired on a 9.4-T small animal MRI (Agilent, Palo Alto, CA, USA) the day after PET/CT (12–14 days after the surgery). Axial T_2 -weighted images using a 2-dimensional fast spin-echo (FSE) sequence (repetition time, $TR = 3000$ ms; echo time, $TE = 10$ ms; effective $TE = 40$ ms; echo train length = 4; number of slices = 29; slice thickness = 1 mm; field-of-view, $FOV = 3.84 \times 3.84$ cm; matrix size = 128×128 ; acquisition time ≈ 3 min) were acquired first to locate the slice that contained the largest tumor cross section. CEST spectra were acquired using a continuous wave pre-saturation pulse (saturation time, $TS = 5$ s; B_1 saturation pulse amplitude = $1 \mu T$; offset frequency pulse alternated between negative and positive, from $-5/+5$ to 0 ppm with 0.2 ppm steps) preceding a series of FSE images acquired on the slice that contained the largest tumor cross-section ($TR = 3$ s, effective $TE = 40$ ms, echo train length = 32, slice thickness = 2 mm, $FOV = 3.84 \times 3.84$ cm FOV , matrix size = 128×128 ; acquisition time ≈ 30 min). Three spectra were obtained from three consecutive 30-min CEST acquisitions. The first CEST spectrum was acquired prior to a 20 % D-glucose infusion. A bolus of 20 % D-glucose solution (0.3 g/kg) was injected at the end of the first spectrum acquisition, following by a 60-min constant infusion of the same 20 % D-glucose solution (1.5 g/kg/h). The acquisition of the second and third CEST spectra corresponded to the first and second half of the constant infusion of glucose, respectively. The CEST imaging workflow is illustrated in Fig. 1b.

All CEST data were analyzed using MATLAB 2018b. A mask of the brain was delineated using the T_2 -weighted MR images and applied to the CEST images. A smoothing spline with a fitting parameter of 0.998 was used to generate Z -spectra at each pixel using all 53 CEST images. B_0 correction was performed by shifting the frequency associated with the Z -spectra minima to 0 ppm. A magnetization transfer ratio asymmetry (MTR_{asym}) spectrum [15] at each pixel is calculated as shown in Eq. (1).

$$MTR_{\text{asym}} = \frac{S(\Delta\omega) - S(-\Delta\omega)}{S_0} \quad (1)$$

The area under the curve (AUC) is calculated using MTR_{asym} (AUC_{MTR}) values from 1.2 to 2.8 ppm [6], and the relative change after glucose infusion is calculated as ΔCEST (see Eq. (2)). Note that $AUC_{\text{(during-infusion)}}$ corresponds to the last 30 min of the glucose infusion (the third CEST spectra), as a different imaging protocol was used in some of the experiments, while the blood glucose was still increasing in the first 30 min of the glucose infusion.

Hyperpolarized $[1-^{13}C]$ pyruvate

Detailed hyperpolarization and imaging procedures can be found in Lim et al. [16]. Rats were transported to a GE Discovery MR750 3.0 T MRI (General Electric Healthcare, Waukesha WI, USA) under anesthesia with 2 % isoflurane immediately after the glucose CEST experiment. An FSE sequence (80×80 mm FOV , 0.3-mm in-plane resolution, 3-mm slice thickness, $TR = 4000$ ms, $TE = 85$ ms, 16 echo trains, and 9 averages) was used to acquire axial T_2 -weighted 1H images which were later used to determine the axial slice(s) that contained the tumor and located at the approximate the same location using the CEST slice information. ProHance gadolinium contrast agent (Bracco Diagnostics, Monroe Township, NJ, USA) was added at a concentration of 1 mM to $[1-^{13}C]$ pyruvate acid (Sigma Aldrich, Miamisburg OH, USA), and the sample was hyperpolarized using a HyperSense dynamic nuclear polarizer (DNP, Oxford Instruments, Abingdon, UK). The resulting buffered hyperpolarized $[1-^{13}C]$ pyruvate solution (80 mM) had a final volume of ~ 4 mL with a pH of 7.4 at $37^\circ C$. A 3-mL volume of hyperpolarized $[1-^{13}C]$ pyruvate solution was rapidly transferred to the MRI where it was injected through a lateral tail vein of the rat in a single 12-second bolus. After waiting a further 13 s for circulation and metabolism, ^{13}C spectra in the axial plane (12×12 spectral imaging matrix, $TR = 80$ ms, bandwidth = 5 kHz, 2048 pts, flip angle = 10°) was acquired using a 2D chemical shift imaging (FID-CSI) pulse sequence (60×60 mm FOV , slice thickness approximately equal to the tumor extent). One FID-CSI with 144 spectra was acquired in each animal with a total scan time of 12 s. Regional maps of the ratio of lactate to pyruvate (Lac:Pyr) were calculated using a customized MATLAB script [16]. The animal was euthanized immediately after the experiment.

Benchtop Blood Glucose Measurement

The blood glucose change was measured by sampling blood from a rat tail artery (weight = 508 g) with a glucometer (Contour 7152B, Bayer HealthCare, Leverkusen, Germany) on the benchtop using the same glucose infusion protocol as the glucoCEST experiment. Baseline blood glucose was measured before the injection of 20 % glucose solution (0.3 g/kg) and the start of a 60-min constant infusion (1.5 g/kg). The blood glucose of the subject was measured every 5 min after the start of glucose infusion.

ROI Selection and Image Registration

Tumor volume was measured on both imaging days using CT perfusion and T₂-weighted MRI datasets, respectively. T₂-weighted MRI was used as guidance for manual delineation of tumor and contralateral brain regions. All voxels that contained tumor were included in the tumor ROIs. The T₂-weighted MRI was also used as a reference to co-register the CT perfusion, CEST, FDG-PET, and hyperpolarized [1-¹³C] pyruvate images using 3D Slicer (www.slicer.org). Manual rigid registration relied on anatomical landmarks identified in both T₂-weighted images (e.g., major white matter features such as the corpus callosum, ventricles, and brain surface), features in the anatomical and perfusion CT (tumour, brain surface, and skull), and uptake in the FDG-PET volume (tumor uptake and normal uptake in the brain, Harderian glands, and surrounding tissue). The T₂-weighted image from the 9.4 T MRI was subsequently used for ROI delineation and applied to all of the co-registered parameter maps (CEST, MRSI, CTP, and FDG-PET). The average BF, BV, and PS values from CT perfusion measurements; average ΔCEST measurement from glucoCEST; SUV from FDG-PET; and Lac:Pyr ratios from hyperpolarized [1-¹³C] pyruvate MRSI in tumor and contralateral brain regions were extracted. An example of registered images and ROIs is shown in Fig. 2.

Statistical Analysis

Paired *T* tests were used to compare the similarity of CT perfusion, CEST, FDG-PET, and hyperpolarized [1-¹³C] pyruvate measurements between the tumor and contralateral brain regions. Paired *T* tests were also performed on the voxel-wise AUC_{MTR} values in the tumor pre-infusion and during infusion in order to determine significant changes in AUC_{MTR} during glucose infusion in each subject. The Pearson correlation between average tumoral CT perfusion parameters, ΔCEST measurement from glucoCEST, SUV from FDG-PET, and Lac:Pyr ratios from hyperpolarized [1-¹³C] pyruvate MRSI was evaluated using IBM SPSS version 22. A *P* value ≤ 0.05 was considered statistically significant.

Results

Tumor Size

As shown in **Supplementary Fig. 1**, the average tumor volume on the day of PET and CT perfusion measurements is 98.4 ± 37.5 mm³ (measured using PS and contrast-enhanced images from CT perfusion), and the average tumor volume on the day of CEST and hyperpolarized [1-¹³C] pyruvate measurements was 99.4 ± 39.5 mm³ (measured in 9.4 T T₂-weighted MRI), with no significant difference in volume between the two imaging days based on a paired *t* test (*P* = 0.54).

Blood Glucose Measurements

Benchtop measurements of blood glucose as a function of time during the glucose infusion protocol are plotted in **Supplementary Fig. 2**. The baseline blood glucose of the subject was 7.3 mmol/L and slowly increased to > 20 mmol/L during the 60-min constant infusion. Blood glucose was 7.6 ± 1.8 mmol/L prior to the FDG-PET and CT perfusion measurements and 6.7 ± 1.3 mmol/L prior to the CEST and hyperpolarized [1-¹³C] pyruvate measurements.

Dynamic CEST Trends

No significant change in applied frequency shifts (*P* = 0.52) was found between pre- (-0.09 ± 0.05 ppm) and during glucose infusion (-0.10 ± 0.04 ppm). Two different trends are observed in the dynamic CEST results (Fig. 3). A significantly increased AUC_{MTR} in the tumor region at 30–60 min during infusion compared to the pre-infusion AUC_{MTR} was denoted as an expected trend (*n* = 5). Significantly decreasing (*n* = 5) or no significant change (*n* = 1) in AUC_{MTR} in the tumor region was denoted as an unexpected trend.

Tumor vs. Contralateral Brain Tissue

After comparing CEST, perfusion, and glycolysis measurements, no statistically significant difference is found in BF and ΔCEST between tumor and contralateral brain tissue (*P* = 0.069 and 0.45, respectively) as shown in Fig. 4a and f (the pixel-wise ΔCEST values in contralateral region that were more than 2 standard deviations away from the mean were discarded as noise); statistically significant increases in BV (*P* < 0.05), PS (*P* < 0.001), SUV (*P* < 0.001), and Lac:Pyr (*P* < 0.001) are found in the tumor region vs. contralateral brain tissue as shown in Fig. 4b–e. The tumor AUC_{MTR} in both pre- and during infusion is significantly higher than the contralateral side (*P* < 0.001) as shown in **Supplementary Fig. 3**.

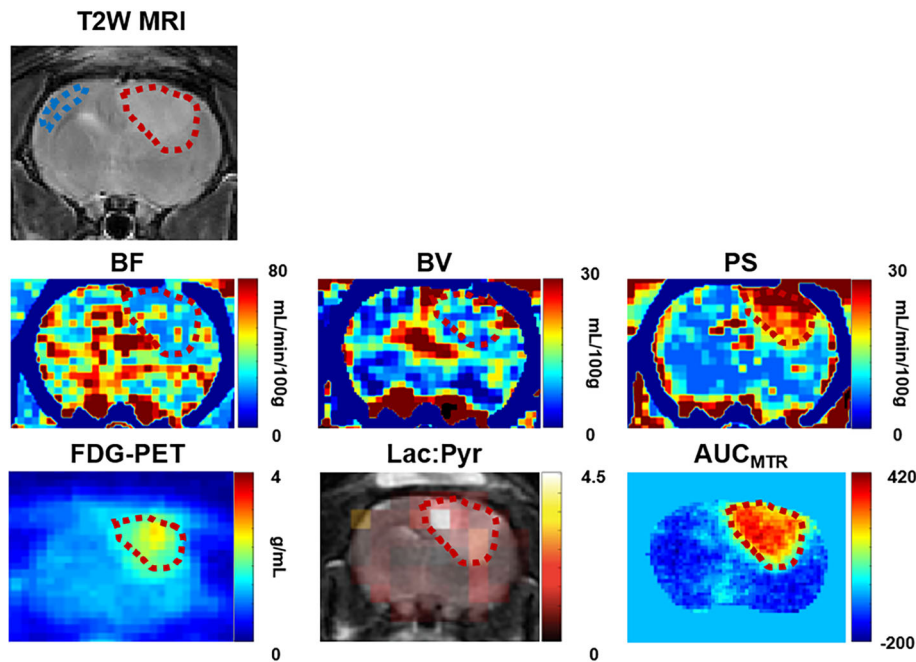


Fig. 2. Example images and ROIs in a single rat. A T_2 -weighted 9.4 T MR image (T2W) was used as a reference to co-register CT perfusion maps (BF, BV, PS), FDG-PET, CEST maps (AUC_{MTR}), and hyperpolarized $[1-^{13}C]$ pyruvate MRSI (Lac:Pyr). The T2W image was subsequently used to delineate tumor (red dotted line) and contralateral brain tissue (blue dotted line), with the same ROI applied to all imaging measurements.

CEST vs. Perfusion and Glycolysis

Δ CEST measurements had statistically significant and strong correlations with CT perfusion measurements of BV (0.74, $P = 0.01$) and PS (0.55, $P = 0.04$); however, no statistically significant correlations were found between BF and Δ CEST ($P = 0.27$). The Pearson correlation

coefficients between Δ CEST and CT perfusion measurements are shown in Table 1. Δ CEST is directly proportional with BV and PS as shown in Fig. 5a and b, respectively.

No statistically significant correlations between Δ CEST and glycolysis measurements using FDG-PET or hyperpolarized $[1-^{13}C]$ pyruvate are found (Table 1).

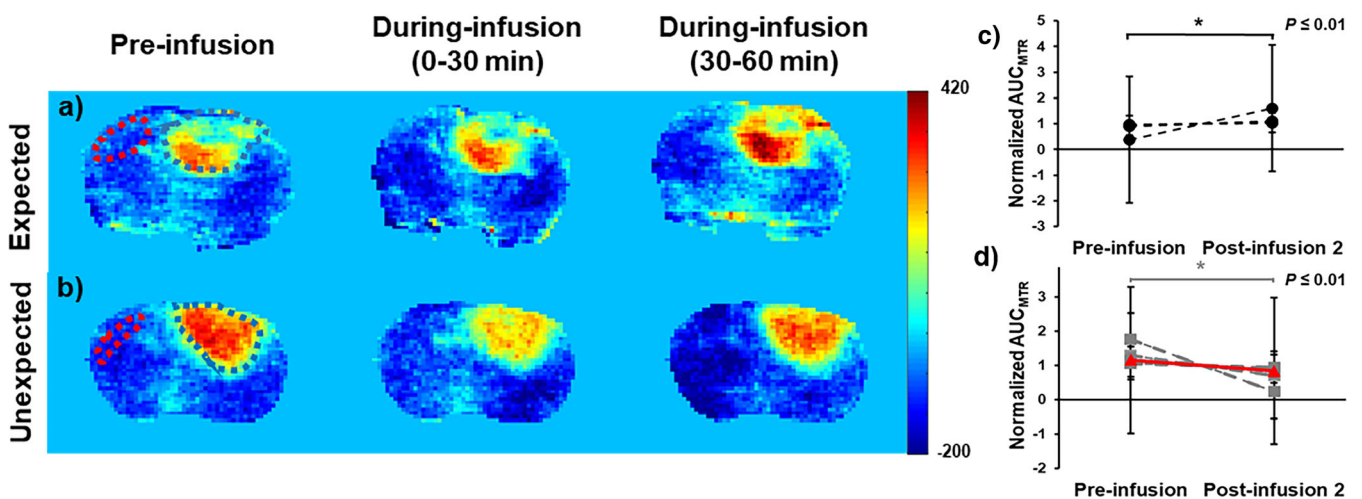


Fig. 3. Illustrative examples of two different trends observed from the dynamic glucoCEST measurements: (a) expected and (b) unexpected change in AUC_{MTR} . The expected trend was observed in 5 subjects and is shown in (c), where during infusion AUC_{MTR} values are significantly higher than pre-infusion AUC_{MTR} . The unexpected trend was observed in 6 subjects and is shown in (d), where during infusion AUC_{MTR} is significantly lower ($n = 5$, grey-dotted line) than or is not significantly different ($n = 1$, red line, $P = 0.46$) from pre-infusion AUC_{MTR} . Error bars = standard deviation.

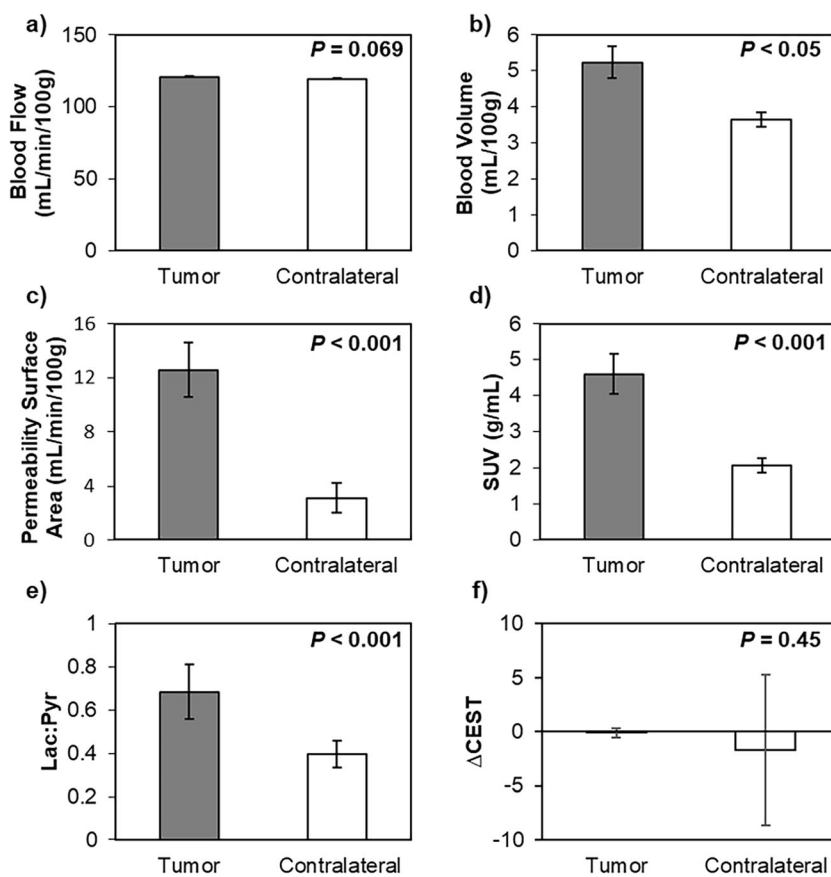


Fig. 4. Mean values from ROIs defined in both tumor and contralateral brain tissue in CT perfusion maps (a) BF, (b) BV and (c) PS, (d) FDG-PET (SUV), (e) hyperpolarized [1-¹³C] pyruvate (Lac:Pyr), and (f) glucoCEST (Δ CEST). A statistically significant ($P < 0.05$) difference was found in BV, PS, SUV, and Lac:Pyr between tumor and contralateral brain. No statistically significant difference was found in BF and Δ CEST between tumor and contralateral brain tissue. Error bars = standard deviation.

Glycolysis vs. Perfusion Measurements

As shown in Table 1, statistically significant moderate correlations between FDG-PET measurements of SUV and CT perfusion measurements of BF (0.49, $P = 0.02$) and PS (0.58, $P = 0.005$) are found. SUV is directly proportional with BF and inversely proportional with PS as shown in Fig. 5c and d, respectively.

Statistically significant moderate correlations between hyperpolarized [1-¹³C] pyruvate measurements of Lac:Pyr and CT perfusion measurements of BV (0.57, $P = 0.02$) and PS (0.75, $P = 0.005$) are also found (Fig. 5e and f).

Table 1. Pearson correlation coefficients between CT perfusion (BF, BV, and PS), FDG-PET (SUV), hyperpolarized [1-¹³C]Pyruvate (Lac:Pyr), and glucoCEST (Δ CEST) measured in the tumor

N = 11	BV				
BF	0.15	BF			
PS	0.57	0.33	PS		
SUV	0.32	0.49*	0.58*	SUV	
Lac:Pyr	0.57*	0.26	0.75*	0.56*	Lac:Pyr
Δ CEST	0.74*	0.24	0.55*	-0.23	0.28

*indicates P value 0.05

As expected, there was a statistically significant moderate correlation between Lac:Pyr and SUV (0.56, $P = 0.038$).

It is important to note that the blood glucose conditions were different prior to the two glycolysis measurements: the average blood glucose level was 7.6 ± 1.8 mmol/L before FDG-PET acquisition, whereas the average blood glucose level was above 33 mmol/L prior to hyperpolarized [1-¹³C] pyruvate MRSI.

Expected vs Unexpected Group

As indicated in **Supplementary Table 1**, in the expected group, a significant correlation between Δ CEST and PS is found (0.60, $P = 0.032$), but no significant correlations were found between other measurements. No significant correlations are found in the unexpected group, as shown in **Supplementary Table 2**.

Discussion

In this study, the association between perfusion and glycolysis was investigated *in vivo* in the C6 rat model

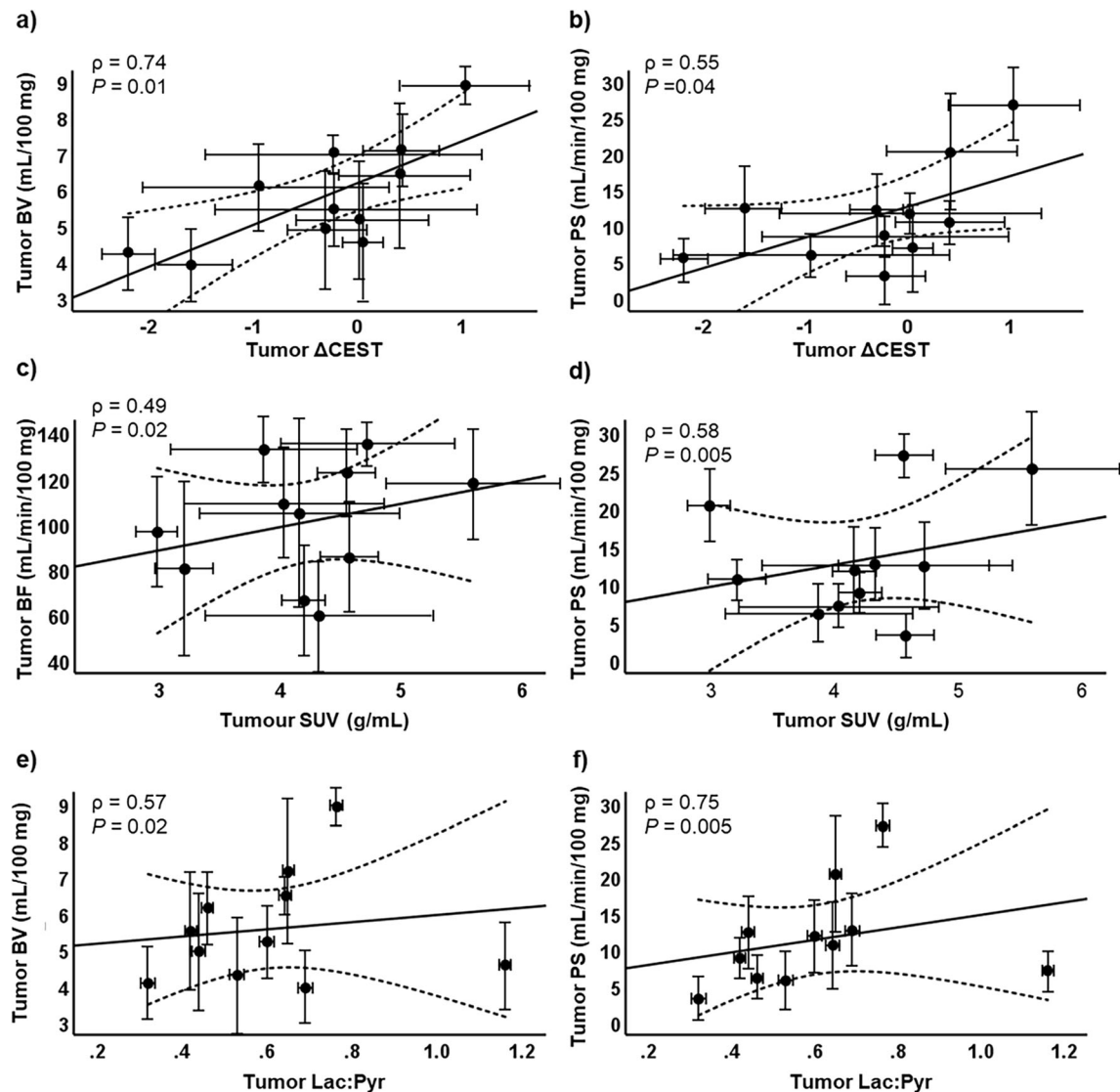


Fig. 5. Δ CEST vs. blood volume (a) and permeability-surface area product (b). Tumor SUV vs. blood flow (c) and permeability-surface area product (d). Tumor Lac:Pyr vs. blood volume (e) and permeability-surface area product (f). Solid line indicates the best fit and the dotted lines denote 95 % confidence interval. Error bar = standard deviation.

using CTP, FDG-PET, glucose CEST, and hyperpolarized [^{13}C] pyruvate MRSI. All imaging experiments were performed within 24 h, and the tumor size did not significantly change within the 24-h span.

Tumor Δ CEST values were both significantly correlated and directly proportional to CT perfusion measurements of BV and PS. Increased BV in the tumor would correspond to a higher blood fraction in the measurement, where glucose concentration will be the highest, and a corresponding increase in glucose available to the tumor—both reflected by increased Δ CEST values. Tumor PS represents the leakiness of the tumor. Higher PS or leakiness would lead to increased glucose delivery throughout the constant infusion of glucose. No significant correlation was found between tumor Δ CEST measurements and tumor perfusion measurements of BF. This could be due to tumor

heterogeneity as brain tumors will contain a mixture of viable, hypoxic, and necrotic regions [17]. The AUC_{MTR} maps generated both pre- and during infusion of glucose most strongly resembled the PS maps, as illustrated in Fig. 6. According to previous work, lower intensity regions on BV and BF maps are associated with tumor necrosis [10]; however, only one subject had an AUC_{MTR} that resembled tumor necrosis co-localized with reduced BV and BF indicative of possible necrosis within the tumor region (Fig. 6 a-c). Studies have shown CEST can distinguish tumor necrosis based on decreased MTR values from amide, attributed to decreased endogenous proteins and peptides in necrotic tissue [18, 19]. CEST measurements from this study could potentially identify tumor necrosis more accurately compared to our CTP measurements of BF and BV as MRI has superior soft tissue contrast [20]. No significant

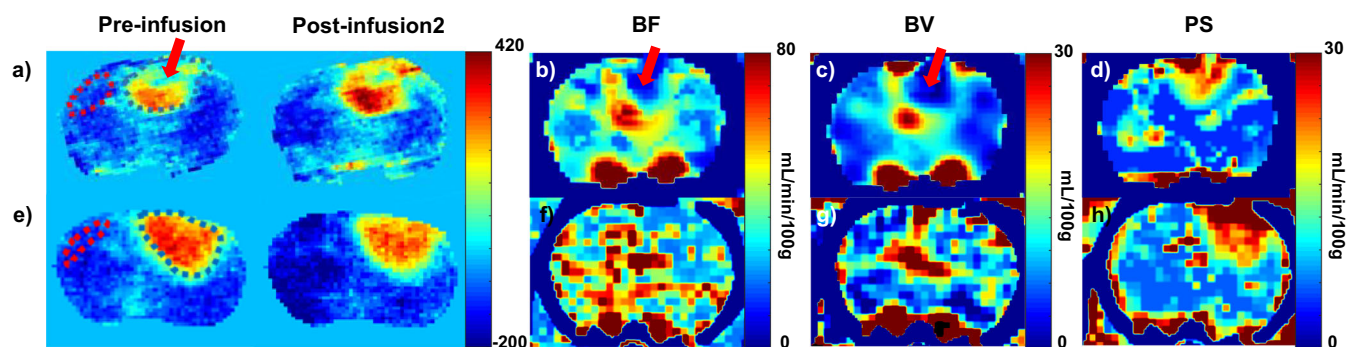


Fig. 6. Good colocalization of the tumor region is displayed in AUC_{MTR} and PS maps. Similarly, co-localization of potential necrosis is shown among AUC_{MTR} , BF, and BV maps (red arrow).

correlations were found between $\Delta CEST$ and tumor glycolysis measurements of SUV or Lac:Pyr ratio. Previous studies have suggested that D-glucose CEST enhancement comes from plasma and extracellular/extravascular spaces [6, 21], whereas SUV and Lac:Pyr ratios will correspond to glucose transport and metabolism in the cell. Our study provides important additional evidence that D-glucose enhanced $\Delta CEST$ is more sensitive to perfusion changes than glycolysis. However, CEST measurements of the immediate response during glucose infusion were missing because CEST experiments for the first 30 min of the glucose infusion were performed with two different protocols.

The tumor perfusion measurements of PS significantly correlated with glycolysis measurements of SUV and Lac:Pyr ratio. PS or leakiness are also related to the aggressiveness of the tumor [22]. Higher PS values (i.e., leakier tumors) are associated with more aggressive tumors, and more aggressive tumors would have a higher metabolism; hence, a directly proportional relationship was found between tumor PS and glycolysis measurements. A moderate but significant correlation was found between tumor BF and SUV and tumor BV and Lac:Pyr ratio. Higher tumor blood flow and blood volume could indicate increased vascularity, allowing more nutrients to be transferred to the tumor for glycolysis. Due to the sequential design of the study, glucose conditions before FDG-PET (normoglycemic) were distinct from the hyperpolarized $[1-^{13}C]$ pyruvate experiment (hyperglycemic) since it was conducted on the next day and immediately followed the glucose CEST experiment; as a result, Lac:Pyr and SUV provided different glycolysis measurements. In a recent study by Hundshammer et al. investigating a subcutaneous breast cancer model in rats, there was moderate correlation between SUV_{mean} and the Lac:Pyr (0.41) that improved when looking at tumors with similar apparent diffusivity coefficients (0.59) [23]. This is quite similar to the correlation we found between SUV and Lac:Pyr (0.56) in our glioma model. Glucose and pyruvate take distinct metabolic pathways [23], which may help explain the moderate but not strong correlation between the two measurements. In our study, hyperglycemia, tumor

glycolytic activity, and lactate production will be elevated during the hyperpolarized $[1-^{13}C]$ pyruvate experiment, while mitochondrial activity and lactate oxidation will be suppressed [24, 25]. Because of the hyperglycemic conditions, more pyruvate produced from glycolysis will be produced and later converted to lactate acid, which may help explain the slightly stronger correlation we found between Lac:Pyr and SUV. Although prolonged hyperglycemic conditions will lead to increased acidity and may eventually lead to saturation of both glucose transport and lactate export in tumor cells, our results, with elevated Lac:Pyr in the tumor and moderate correlation between Lac:Pyr and SUV, suggest that there is still elevated conversion of pyruvate to lactate, even in the hyperglycemic conditions present in the experiment.

The dynamic changes of AUC_{MTR} for all subjects are shown in Fig. 3c. Two different trends are found from the dynamic CEST experiment as shown in Fig. 3a and b. The expected trend illustrated an increasing intensity over the time of glucose infusion in the tumor region, assuming the glucose solution would act as either a glucose metabolism or perfusion contrast agent. An increase of glucose CEST signal in the tumor region was expected due to the increased glucose concentration caused by a constant infusion of glucose. Dynamic CEST maps at later infusion times appear to enhance the boundary between necrotic and viable tumor areas as shown in Fig. 3a. The glucose infusion captured the leaky vessels of the viable tumor region, helping to facilitate glucose perfusion and enhancing the contrast between viable tumor and necrotic tumor areas. In some cases, however, the CEST map would decrease after the start of the glucose infusion (Fig. 3b). The mechanisms for the unexpected decrease in CEST signal need to be elucidated in future studies but may be related to the complex vascularity of the tumor, the insulin response, and/or changes in tumor pH induced by the glucose infusion.

There are several limitations for this experiment. Large tumors will often encompass the ventricles; as a result, the ROI defined using the T_2 -weighted MRI will contain CSF. The inclusion of CSF in tumor ROIs could lead to underestimation of all measurements in the tumor regions

as CSF is distinct from the contrast agent in the blood vessels and tissue. Although histology was not performed, in a previous study using the same C6 tumor model [10], we demonstrated the relationship between tumor perfusion measurements and tumor hypoxia and necrosis using CT perfusion and corresponding histology data. We found that CT perfusion measurements of BF and BV are associated with tumor necrosis and hypoxia: regions with higher values of BF and BV representing viable tumor would surround regions with lower values of BF and BV, which were associated with lack of vascularization due to tumor hypoxia, necrosis, or fibrosis [26]. T₂-weighted MRI offers better soft tissue contrast and resolution for tumor delineation; however, the delineated region could potentially include non-tumor features such as edema [27]. Fasting was not done prior to FDG-PET or subsequent glucoCEST and hyperpolarized [1-¹³C] pyruvate MRSI experiments; instead, blood glucose was monitored and confirmed to be within the normoglycemic range prior to both imaging experiments. Although this could potentially decrease FDG uptake [28], there is evidence that glucose loading conditions may actually increase the conspicuity of brain tumors as normal brain uptake is decreased, but gliomas continue to utilize FDG, even in hyperglycemic conditions [29]. Fasting for an extended period of time in small animals may also have more significant deleterious consequences than in humans, particularly if repeated for 2 days in a row for both imaging experiments [30]. Finally, in humans, FDG uptake has been shown to be approximately the same across brain regions in hypo- and normoglycemic conditions [31]. Ultimately, we chose to monitor blood glucose instead of applying a fasting protocol prior to both imaging days in this fragile animal model. Blood glucose levels were comparable prior to the start of both imaging experiments, and FDG uptake was conspicuous in the tumor relative to the surrounding brain tissue.

Although the imaging measurements were conducted within 24 h, they were in the span of 2 days, and on multiple scanners, as a result, the tumor perfusion and glycemic environment were not identical during the measurements. During the hyperpolarized [1-¹³C] pyruvate MRSI experiment, the subject will have received a relatively large injected volume that includes both the previous constant infusion of glucose and a bolus of [1-¹³C] pyruvate (approximately 6 mL total). Hypervolemia could lead to an elevated BV and PS [32, 33]; however, BF should not be significantly affected [32]. Renal function such as the glomerular filtration rate will be elevated during glucose infusion [34] in order to compensate for the volume increase. The study plan was designed to follow the radiation safety protocol at different sites; as a result, the subjects had to be housed at our PET facility overnight to allow the radioactivity to decay before the subjects could be transferred to the MR facility. A hybrid PET/MR system could be used in the future to provide simultaneous measurement under the same tumor microenvironment.

Meanwhile, there are a number of factors that could affect the CEST signal, including pH [35, 36]. A lower pH environment would be induced by hyperglycemia [37] and in turn will lead to decreased CEST signal [6]. The glucose CEST measurements (AUC_{MTR}) during the constant infusion of glucose would have been underestimated due to pH reduction under hyperglycemic conditions. The effect of hyperglycemia on the tumor pH environment induced by a constant infusion of glucose needs to be further investigated. One approach may be to use pH-sensitive CEST acquisitions such as acidoCEST [38, 39] or amine and amide concentration-independent detection (AACID) [40] in conjunction with an infusion of glucose. The role that mammalian target of rapamycin (mTOR) plays in glucoCEST was not identified in this study. mTOR is upregulated in aggressive tumors and leads to elevated glucose uptake [41]. During the last half of the infusion protocol (during infusion), tumor metabolism is likely to have plateaued as excess amounts of glucose are introduced into the system. In this scenario, glucoCEST would predominantly reflect perfusion effects. Xu et al. also concluded that glucoCEST signal originates mainly from the extravascular/extracellular space and blood vessels [41]. There are a couple of additional limitations using D-glucose as a contrast agent for CEST signal enhancement. The metabolism of glucose in cells will decrease glucoCEST signal as the metabolites from glycolysis cannot be detected with CEST [42]. In addition, insulin response to high blood glucose concentration will limit the amount of detectable free glucose in blood [42, 43].

Conclusions

Dynamic glucose CEST measurements of tumor Δ CEST was significantly correlated with tumor perfusion measurements of BV and PS but not tumor glycolysis measurements of SUV and Lac:Pyr, suggesting that glucose CEST imaging using Δ CEST functions primarily as a perfusion tracer. Conversely, tumor glycolysis measurements of SUV and Lac:Pyr were significantly correlated with perfusion measurements of PS, reflecting increased tumor leakiness in tumors with higher glycolytic metabolism. Confounding these results is the fact that hyperglycemia induced by a constant infusion of glucose during dynamic CEST experiments may lead to a more acidic pH environment and give rise to underestimation of CEST measurements. Subsequently, in approximately half of the dynamic glucose CEST experiments, there was a drop in CEST signal post-glucose infusion. Although glucose CEST measurements may yield additional novel information about tumor status, the complicated dependency of glucose CEST signal on a variety of factors would benefit from additional *in vivo* mechanistic studies.

Supplementary Information. The online version contains supplementary material available at <https://doi.org/10.1007/s11307-021-01585-1>.

References

1. Wen PY, Kesari S (2008) Malignant gliomas in adults. *N Engl J Med* 359:492–507
2. Jain RK, di Tomaso E, Duda DG, Loeffler JS, Sorensen AG, Batchelor TT (2007) Angiogenesis in brain tumors. *Nat Rev Neurosci* 8(8):610–622
3. Sagiyama K, Mashimo T, Togao O, Vemireddy V, Hatanpaa KJ, Maher EA, Mickey BE, Pan E, Sherry AD, Bachoo RM, Takahashi M (2014) In vivo chemical exchange saturation imaging allows early detection of a therapeutic response in glioblastoma. *Proc Natl Acad Sci U S A* 111(12):4542–4547
4. Chan KW, McMahon MT, Kato Y et al (2012) Natural D-glucose as a biodegradable MRI contrast agent for detecting cancer. *Magn Reson Med* 68(6):1764–1773
5. Torrealdea F (2016) Investigation of brain tumor metabolism using naturally occurring chemical exchange saturation transfer agents with magnetic resonance imaging. PhD Thesis, University College London
6. Walker-Samuel S, Ramasawmy R, Torrealdea F, Rega M, Rajkumar V, Johnson SP, Richardson S, Gonçalves M, Parkes HG, Årstad E, Thomas DL, Pedley RB, Lythgoe MF, Golay X (2013) In vivo imaging of glucose uptake and metabolism in tumors. *Nat Med* 19(8):1067–1072
7. Jin T, Mehrens H, Hendrick KS, Kim SG (2014) Mapping glucose uptake with chemical exchange-sensitive spin-lock magnetic resonance imaging. *J Cerebral Metab* 34:1402–1410
8. Xu X, Yadav N, Knutsson L et al (2015) Dynamic glucose-enhanced (DGE) MRI: translation to human scanning and first results in glioma patients. *Tomography* 1(2):105–114
9. Jin T, Lordanova B, Hitchens TK et al (2018) Chemical exchange-sensitive spin-lock (CESL) MRI of glucose and analogs in brain tumors. *MR Med* 80:488–495
10. Qi Q, Yeung TPC, Lee TY, Bauman G, Cruckley C, Morrison L, Hoffman L, Yartsev S (2016) Evaluation of CT perfusion biomarkers of tumor hypoxia. *PLoS One* 11(4):e0153569
11. Yeung TPC, Wang Y, He W et al (2015) Survival prediction in high-grade gliomas using CT perfusion imaging. *J Neuro-Oncol* 123:93–123
12. Yeung TPC, Bauman G, Yartsev S, Fainardi E, Macdonald D, Lee TY (2015) Dynamic perfusion CT in brain tumors. *Eur J Radiol* 84(12):2386–2392
13. Lee TY, Purdie TG, Stewart E (2003) CT imaging of angiogenesis. *QJ Nucl Med* 41:171–187
14. Tahari AK, Chien D, Azadi J et al (2014) Optimum lean body formulation for correction of standardized uptake value in PET imaging. *JNM* 55:1481–1484
15. Liu G, Song X, Chan KW et al (2013) Nuts and bolts of chemical exchange saturation transfer MRI. *NMR Biomed* 26(7):810–828
16. Lim, H (2017) A Longitudinal study of tumor metabolism using hyperpolarized carbon-13 magnetic resonance spectroscopic imaging in a preclinical model of glioma. PhD Thesis, Western University, London
17. Bonavia R, Inda M, Cavanee WK et al (2011) Heterogeneity maintenance in glioblastoma: a social network. *Cancer Res* 71:4055–4060
18. Mehrabian H, Desmon KL, Soliman H et al (2017) Differentiation between radiation necrosis and tumor progression using chemical exchange saturation transfer. *Clin Cancer Res* 23:3667–3675
19. Zhou J, Tryggstad E, Wen Z, Lal B, Zhou T, Grossman R, Wang S, Yan K, Fu DX, Ford E, Tyler B, Blakeley J, Laterra J, van Zijl P (2010) Differentiation between glioma and radiation necrosis using molecular magnetic resonance imaging of endogenous proteins and peptides. *Nat Med* 17(1):130–134
20. Hogeboom WR, Hoekstra HJ, Mooyaart EI et al (1991) MRI and CT in the preoperative evaluation of soft-tissue tumors. *Arch Orthop Trauma Surg* 110:162–164
21. Xu X, Chan K, Knutsson L et al (2015) Dynamic glucose enhanced (DGE) MRI for combined imaging of blood-brain barrier break down and increased blood volume in brain cancer. *Magn Reson Med* 74:1556–1563
22. Cao Y, Nagesh V, Hasmstra D et al (2006) The extent and severity of vascular leakage as evidence of tumor aggressiveness in high-grade gliomas. *Cancer Res* 66(17):8912–8917
23. Hundershhammer C, Braeuer M, Müller CA et al (2018) Simultaneous characterization of tumor cellularity and the Warburg effect with PET, MRI and hyperpolarized ¹³C-MRSI. *Theranostics* 8(17):4765–4780
24. Twarock S, Reichert C, Peters U, Gorski DJ, Röck K, Fischer JW (2017) Hyperglycemia and aberrated insulin signaling stimulate tumor progression via induction of extracellular matrix component hyaluronan. *Int J Cancer* 141:791–804
25. Lund J, Ouwens DM, Wettergreen M et al (2019) Increased glycolysis and higher lactate production in hyperglycemic myotubes. *Cells* 8(9):1101. <https://doi.org/10.3390/cells8091101>
26. Hsu T, Nguyen-Tran HH, Trojanowska M (2019) Active roles of dysfunctional vascular endothelium in fibrosis and cancer. *J Biomed Sci* 26:86
27. Blystad I, Wartjes JBM, Smedby Ö, Lundberg P, Larsson EM, Tisell A (2017) Quantitative MRI for analysis of peritumoural edema in malignant gliomas. *PLoS ONE* 12(5):e0177135. <https://doi.org/10.1371/journal.pone.0177135>
28. Furger BJ, Czernin J, Hildebrandt, et al. (2006) Impact of animal handling on the results of ¹⁸F-FDG PET study in mice. *J Nucl Med* 47(6):999–1006
29. Kim D, Ko HY, Lee S, Lee YH, Ryu S, Kim SY, Chung JI, Lee M, Moon JH, Chang JH, Yun M (2020) Glucose loading enhances the value of 18F-FDG PET/CT for the characterization and delineation of cerebral gliomas. *Cancers* 12(7). <https://doi.org/10.3390/cancers12071977>
30. Jensen TL, Kiersgaard MK, Sørensen DB, Mikkelsen LF (2013) Fasting of mice: a review. *Lab Anim* 47(4):225–240
31. Sarikaya I, Albatineh AN, Sarikaya A (2020) Effect of various blood glucose levels on regional FDG uptake in the brain. *Asia Ocean J Nucl Med Biol* 8(1):46–53
32. Todd MM, Weeks JB, Warner DS (1993) The influence of intravascular volume expansion on cerebral blood flow and blood volume in normal rats. *Anesthesiology* 78:945–953
33. Cole DJ, Drummond JC, Mastumura JS et al (1990) Hypervolemic-hemodilution and hypertensive during temporary middle cerebral artery occlusion in rats: the effect on blood-brain barrier permeability. *Can J Neurol Sci* 17:372–377
34. Christiansen JS, Frandsen M, Parving HH (1981) Effect of intravenous glucose infusion on renal function in normal man and insulin-dependent diabetics. *Diabetologia* 21:368–373
35. van Zijl PCM, Yadav NN (2011) Chemical exchange saturation transfer (CEST): What is in a name and what isn't? *Magn Reson Med* 65(4):927–948
36. Sun PZ, Sorensen AG (2008) Imaging pH using the chemical exchange saturation transfer (CEST) MRI: Correction of concomitant RF irradiation effects to quantify CEST MRI for chemical exchange rate and pH. *Magn Reson Med* 60(2):390–397
37. Roszinski S, Wiedemann G, Jiang SZ, Baretton G, Wagner T, Weiss C (1991) Effects of hyperthermia and/or hyperglycemia on pH and pO₂ in well oxygenated xenotransplanted human sarcoma. *Int J Radiat Oncol Biol Phys* 20(6):1273–1280
38. Chen LQ, Howison CM, Jeffery JJ, Robey IF, Kuo PH, Pagel MD (2014) Evaluation of extracellular pH within *in vivo* tumors using acidoCEST MRI. *Magn Reson Med* 72(5):1408–1417
39. Longo DL, Bartoli A, Consolino L, Bardini P, Arena F, Schwaiger M, Aime S (2016) In vivo imaging of tumor metabolism and acidosis by combining PET and MRI-CEST pH imaging. *Cancer Res* 76(22):6463–6470
40. McVicar N, Li A, Gonçalves DF et al (2014) Quantitative tissue pH measurement during cerebral ischemia using amine and amide concentration-independent detection (AACID) with MRI. *J Cereb Blood Flow Metab* 34(4):690–698
41. Xu X, Xu J, Knutsson L, et al. (2019) The effect of the mTOR inhibitor rapamycin on glucoCEST signal in a preclinical model of glioblastoma. *Magn Reson Med* 81(6):3798–3807
42. Nasrallah FA, Pages G, Kuchel PW et al (2013) Imaging brain deoxyglucose uptake and metabolism by glucoCEST MRI. *J Cereb Blood Flow Metab* 33:1270–1278
43. Sehgal AA, Li Y, Lal B et al (2018) CEST MRI of 3-O-methyl-D-glucose and accumulation in brain tumors. *Magn Reson Med* 81:1993–2000